J. Fluid Mech. (2020), *vol*. 901, A24. © The Author(s), 2020.
Published by Cambridge University Press
doi:10.1017/jfm.2020.573

Solute dispersion in bifurcating networks

Robert A. Zimmerman[1] **and Daniel M. Tartakovsky**[2],†

[1]Los Alamos National Laboratory, Los Alamos, NM 87545, USA

[2]Department of Energy Resources Engineering, Stanford University, 367 Panama Street, Stanford, CA 94305, USA

(Received 6 March 2020; revised 26 May 2020; accepted 6 July 2020)

Advective–diffusive transport of passive scalars in confined environments (e.g. vessels and channels) within a network is of fundamental importance in a plethora of biological and geophysical phenomena. We conduct a leading-order analysis, consistent with the theory of hydrodynamic dispersion, which averages out the radial variability within a vessel. One-dimensional solutions for individual vessels (edges of a network), obtained for arbitrary (undefined) transient Dirichlet boundary conditions, serve as a building block for a network model. A network transport solution is developed by iteratively linking single-vessel solutions to each other in a bifurcating fractal tree model, i.e. at nodes of the network. We find transport behaviour to be strongly affected by the network geometry and daughter vessels to significantly impact the rate of transport in the upstream parent vessels.

Key words: biomedical flows, porous media

1. Introduction

Advective–diffusive transport in networks is ubiquitous in natural and engineered systems. These include geophysical phenomena such as heat transfer (Gisladottir, Roubinet & Tartakovsky 2016) and solute transport (Roubinet, de Dreuzy & Tartakovsky 2013) in fractured rocks, and transport of metabolically critical substances through networks of tubes or channels contained in most multicellular organisms. Examples of the latter are transport in xylem and phloem networks (Minamino & Tateno 2014), floral networks (Young, Evert & Eschrich 1973; McCulloh, Sperry & Adler 2003; Sack & Holbrook 2006) and fungal networks (Jennings 1987; Cairney 1992); oxygen transport through the cardiovascular system (Goldman & Popel 2000; Beard & Bassingthwaighte 2001; Goldman 2008); and drug delivery (Shipley & Chapman 2010).

The cardiovascular system is an intricate and complex network of blood vessels with a wide range of geometries and rheological flow properties. For example, whole blood, which is a composition of plasma and suspended particles (e.g. erythrocytes and leukocytes), is a non-Newtonian fluid that behaves as a Newtonian fluid in large (relative to erythrocyte diameter) blood vessels (Hellums *et al.* 1995; Sriram, Intaglietta & Tartakovsky 2014*a*). High-fidelity three-dimensional analyses of such a network are extraordinarily complex and computationally expensive (Olufsen 1999). However, subsections of the cardiovascular network approximately propagate in fractal patterns

† Email address for correspondence: tartakovsky@stanford.edu

(Olufsen 1999), which facilitates modelling efforts. Furthermore, higher-dimensional solutions for a single blood vessel seldom provide significantly more information to network transport problems than one-dimensional models.

For a one-dimensional solution to the advection–dispersion equation in a finite-length vessel to serve as a building block in a network model, it must handle arbitrary transient Dirichlet boundary conditions at the vessel's inlet and outlet. Previous models have used semi-infinite solutions to describe transport in vessels embedded in networks (Gentile, Ferrari & Decuzzi 2008). The semi-infinite assumption for transport in embedded vessels does not account for the impedance incurred in the vessel's outlet due to diminishing diameters in downstream vessels. Instead, our analysis relies on a closed-form Laplace-transformed analytical solution to the advection–dispersion equation in a bounded domain, and on its numerical inversion. This solution, written for each vessel in a network, is coupled at the network's edges by enforcing the continuity of mass and momentum, i.e. the continuity of solute concentration and mass flux between the adjacent vessels.

This strategy is applicable to two popular network types. The first is a lattice network, which is widely used in studies of natural porous media (Roubinet *et al.* 2013; Gisladottir *et al.* 2016). Lattice-like structures allow flow to conjoin and bifurcate throughout the entire network (Bruderer & Bernabé 2001); these models might be appropriate for transport through organic tissue similar to the cardiovascular capillary bed (Beard & Bassingthwaighte 2000, 2001). The second type is a bifurcating fractal network, such as the arterial tree in the cardiovascular system (Olufsen 1999; Olufsen *et al.* 2000; Cousins & Gremaud 2012; Cousins, Gremaud & Tartakovsky 2013). An analytical treatment of the flow in such networks, which accounts for outflow boundary effects due to a downstream bifurcating network, was developed by Cousins & Gremaud (2012) and Cousins *et al.* (2013). In the context of transport in fungal structures, Heaton *et al.* (2012*a*,*b*) provided a nodal solution in Laplace space. The latter model assumes a linear concentration distribution between the nodes and thus does not give a rigorous description of concentration distribution along network edges. We develop an edge-wise solution, which overcomes this simplification by treating the nodal concentrations as the outlet and inlet boundary conditions for the finite-length vessel solutions.

Section 2 contains a formulation of the fractal tree model, and collates our modelling assumptions. In § 3 we present solutions to the one-dimensional advection–dispersion transport equations in finite and semi-infinite vessels. These solutions are assembled together in § 4 to describe hydrodynamic dispersion of passive solutes in fractal bifurcating networks. Section 5 presents the results of the network model for sinusoidal and constant inlet network boundary conditions. Major conclusion drawn from our study are summarized in § 6.

2. A network model

We consider dispersion of a passive scalar by an incompressible Newtonian fluid flowing through a bifurcating network. Our network choice is motivated by the cardiovascular system comprising a wide variety of vessels (table 1), whose diameter ranges from 8 μm to 10 mm (Zamir 1988; Adam 2011). Because blood consists of particles (in particular, erythrocytes and leukocytes) suspended in plasma, its rheological behaviour changes as it transits through the cardiovascular network from larger to smaller vessels due to the Fahraeus–Lindqvist effect (Pries *et al.* 1990; Sriram *et al.* 2014*a*). This phenomenon significantly affects radial transport through vessel walls and the flow profile. However, our analysis treats vessel walls as impermeable. Changes in viscosity, affecting the flow velocity profile, do not significantly change the average density of blood in vessels with

Level	Vessel description	No. of vessels	L (cm)	$2a$ (mm)	λ	α
1	aorta	1	40	10	0.0125	—
2	large arteries	40	20	3	0.075	0.3
3	main branches	600	10	1	0.005	0.33
4	secondary branches	1.8×10^3	4	0.6	0.0075	0.6
5	tertiary branches	7.6×10^4	1.4	0.14	0.005	0.233
6	terminal arteries	10^6	0.1	0.05	0.025	0.357
7	terminal branches	1.3×10^7	0.15	0.03	0.01	0.600
8	arterioles	4×10^7	0.2	0.02	0.005	0.666
9	capillaries	1.2×10^9	0.1	0.008	0.004	0.4

TABLE 1. Dimensions of the cardiovascular vessels (Zamir 1988; Adam 2011). Here, $\lambda = a/L$ is the ratio between the radius (a) and length (L) of a vessel; and $\alpha = a_d/a_p$ is the ratio between the radii of the daughter (a_d) and parent (a_p) vessels.

diameter larger than 15 μm (Hellums *et al.* 1995; Sriram *et al.* 2014*a*, and the references therein) and, with some reservations, as small as 8 μm (Goldman 2008). We restrict our analysis to vessels with diameter greater than 13.8 μm.

In large vessels of the cardiovascular network, flow is as periodic as the beating of the heart. In large arteries, flow is variable along the length of an artery as the vessel diameter tapers. Transport in such arteries must be modelled individually (Olufsen 1999), as the geometry of the vessel and elasticity of the vessel wall have significant impacts on the pattern of fluid flow. However, further downstream, in the arteriolar tree, flow becomes steady (Green 1944; Sarpkaya 1966). These vessels, tertiary branches to arterioles, are a part of the arteriolar network that may be modelled as a fractal tree (Olufsen 1999; Olufsen *et al.* 2000; Cousins & Gremaud 2012; Cousins *et al.* 2013). Based on the preceding discussion, we make the following assumptions about flow in the arteriolar tree:

(i) blood flow in arterioles behaves as a Newtonian fluid (Lee & Fung 1971; Zimmerman *et al.* 2019);
(ii) the vessels are modelled as straight cylinders with rigid walls;
(iii) flow in arterioles is characterized by low Reynold's numbers and, as such, exhibits a laminar Poiseuille profile (Green 1944; Sarpkaya 1966); and
(iv) the arteriolar vessels are far downstream from the heart and the flow is well mixed (i.e. axial variations are negligible) and steady (Womersley 1955; Lee & Fung 1971).

2.1. *Fractal model of the arteriolar network*

Following Olufsen (1999) and others, we adopt a fractal model of the arteriolar network in which each parent vessel of radius a bifurcates into two smaller daughter vessels. Each vessel generation bifurcates until a minimum radius a_{min} is reached at the terminal daughter vessels. Murray's law states that the fractal arteriolar tree satisfies the principle of minimum work (Uylings 1977). It gives rise to a relationship between the radii of the parent (a_p) and daughter (a_{d_1} and a_{d_2}) vessels,

$$a_p^\zeta = a_{d_1}^\zeta + a_{d_2}^\zeta. \tag{2.1}$$

The exponent ζ is estimated to be $\zeta = 2.76$ in the human cardiovascular system (Olufsen 1999).

Let α_1 and α_2 denote the ratios between the radii of the daughter vessels and the radius of the parent vessel,

$$a_{d_1} = \alpha_1 a_p, \quad a_{d_2} = \alpha_2 a_p. \tag{2.2a,b}$$

It follows from (2.1) and (2.2*a*,*b*) that

$$\alpha_1 = (1 + \psi^\zeta)^{-1/\zeta}, \quad \alpha_2 = \psi\alpha_1, \quad \psi = a_{d_2}/a_{d_1}. \tag{2.3a–c}$$

To simplify the presentation, we consider symmetric bifurcations, i.e. set the asymmetry ratio to $\psi = 1$, so that $\alpha_1 = \alpha_2 \equiv \alpha = 2^{-1/\zeta}$. The fractal behaviour means that the parent–daughter scaling (2.2*a*,*b*) holds across all the generations,

$$\frac{a_{k+1}}{a_k} = \alpha = 2^{-1/\zeta}, \tag{2.4}$$

where k denotes the vessel generation.

2.2. *Flow in fractal arteriolar networks*

A relation for the flow velocities in the parent and daughter vessels is derived from the continuity equation. The mass flow rate, $\dot{m}_k$, in a vessel of kth generation is given by

$$\dot{m}_k = \frac{\pi}{4}\rho a_k^2 v_k, \tag{2.5}$$

where ρ is the fluid density and v is the average flow speed (Darcy flux). For symmetrically bifurcating trees, mass continuity yields

$$\dot{m}_k = 2\dot{m}_{k+1}. \tag{2.6}$$

We treat the fluid density ρ as constant throughout the entire arteriolar tree under consideration, because variations in density due to the Fahraeus–Lindqvist effect are minimal (Pries *et al.* 1990; Sriram *et al.* 2014*a*). Combining (2.4)–(2.6), we obtain the relationship for flow speed in two adjacent generations,

$$v_{k+1} = \frac{v_k}{2\alpha^2}. \tag{2.7}$$

3. Solute transport in individual vessels

Analytical solutions presented in this section express the concentration distribution within an individual vessel in terms of the (unknown, time-varying) nodal concentrations. The vessel's length and radius are L and a, respectively.

3.1. *Problem formulation*

Following Fung & Tang (1975) and Berg *et al.* (2020) among many others, we assume that solute concentration in a single vessel, $C(x, r, t)$, satisfies an advection–diffusion equation,

$$\frac{\partial C}{\partial t} = D_m\left[\frac{1}{r}\frac{\partial}{\partial r}\left(r\frac{\partial C}{\partial r}\right) + \frac{\partial^2 C}{\partial x^2}\right] - u(r)\frac{\partial C}{\partial x}, \tag{3.1}$$

where $x \in (0, L)$ and $r \in (0, a)$ are the axial and radial coordinates, respectively; $t > 0$ is time; $u(r)$ is the flow velocity given by the Poiseuille law; and D_m is the coefficient of

molecular diffusion. This equation is subject to initial and boundary conditions

$$\left.\begin{aligned} &C(x,r,0)=c_{in}, \quad C(0,r,t)=c_0(t), \quad C(L,r,t)=c_L(t),\\ &C(x,0,t)<\infty, \quad \frac{\partial C}{\partial r}(x,a,t)=0. \end{aligned}\right\} \tag{3.2a–e}$$

The last condition implies that vessel walls are impermeable to the solute. With the important caveats described in the Introduction, this assumption renders the results presented below relevant to such applications as targeted drug delivery (Shaw & Murthy 2010); transport of some contrast agents used for *in vivo* molecular neuroimaging (Koffie *et al.* 2011); and dispersion of large molecules such as PEG-haemoglobin and PEG-albumin proposed for use as blood substitutes (Cabrales *et al.* 2005) or high molecular weight hydroxyethyl starches used as plasma expanders (Dailey *et al.* 2005). In these and other similar applications, the initial condition in (3.2*a–e*) represents a step concentration increase at the onset of an intervention. Finally, the imposition of the Dirichlet boundary conditions at the vessel's inlet and outlet facilitates the use of the solution to (3.1)–(3.2*a–e*) as a building block for the network solution developed in § 4.

For solutes that permeate vessel walls, the analytical solution of Zimmerman, Severino & Tartakovsky (2018) can replace the solution to (3.1)–(3.2*a–e*) in the construction of the network solution.

3.2. *Advection–dispersion equation*

For physiologically relevant conditions, $a \ll L$ and the radial dependence of solute concentration plays an insignificant role in the solute migration through the network. Therefore, we are interested in the dynamics of cross-sectionally averaged concentration

$$C_{av}(x,t)=\frac{2}{a^2}\int_0^a C(x,r,t)r\,\mathrm{d}r. \tag{3.3}$$

The latter satisfies an advection–dispersion equation (Aris 1956)

$$\frac{\partial C_{av}}{\partial t}=D\frac{\partial^2 C_{av}}{\partial x^2}-v\frac{\partial C_{av}}{\partial x}, \quad v\equiv\frac{2}{a^2}\int_0^a u(r)r\,\mathrm{d}r, \quad D=D_m+\frac{v^2a^2}{192D_m}. \tag{3.4a–c}$$

This equation is subject to the initial and boundary conditions

$$C_{av}(x,0)=c_{in}, \quad C_{av}(0,t)=c_0(t), \quad C_{av}(L,t)=c_L(t). \tag{3.5a–c}$$

Let L_c, v_c, D_c and c_c denote the maximum values of the vessel length, Darcy velocity, dispersion coefficient and solute concentration in the network, respectively. We define dimensionless independent and dependent quantities,

$$\left.\begin{aligned} &\bar{t}=\frac{tD}{L_c^2}, \quad \bar{x}=\frac{x}{L_c}, \quad \bar{L}=\frac{L}{L_c}, \quad \bar{v}=\frac{v}{v_c}, \quad \bar{D}=\frac{D}{D_c}, \quad Pe=\frac{v_cL_c}{D_c},\\ &\bar{C}_{av}=\frac{C_{av}}{c_c}, \quad \bar{c}_{in}(\bar{x})=\frac{c_{in}(\bar{x})}{c_c}, \quad \bar{c}_L(\bar{t})=\frac{c_L(\bar{t})}{c_c}, \quad \bar{c}_0(\bar{t})=\frac{c_0(\bar{t})}{c_c}. \end{aligned}\right\} \tag{3.6a–j}$$

A dimensionless form of (3.4*a–c*) and (3.5*a–c*) takes the form

$$\frac{\partial \bar{C}_{av}}{\partial \bar{t}}=\bar{D}\frac{\partial^2 \bar{C}_{av}}{\partial \bar{x}^2}-Pe\,\bar{v}\frac{\partial \bar{C}_{av}}{\partial \bar{x}}, \quad \bar{x}\in(0,\bar{L}), \quad \bar{t}>0, \tag{3.7}$$

with

$$\bar{C}_{av}(\bar{x},0)=\bar{c}_{in},\quad \bar{C}_{av}(0,\bar{t})=\bar{c}_0(\bar{t}),\quad \bar{C}_{av}(\bar{L},\bar{t})=\bar{c}_L(\bar{t}). \tag{3.8a–c}$$

In the remainder of this study we utilize the dimensionless quantities but drop the bar $^-$ to simplify the notation.

3.3. *Concentration distributions within a single vessel*

We show in appendix A that the Laplace-transformed solution of (3.7) and (3.8*a–c*) is

$$\hat{C}_{av}(x,s)=\mathrm{e}^{\gamma x}\frac{\sinh[(L-x)\Gamma]\hat{c}_0(s)+\mathrm{e}^{-\gamma L}\sinh(x\Gamma)\hat{c}_L(s)}{\sinh(L\Gamma)} + \frac{2Dc_{in}}{L}\mathrm{e}^{\gamma x}\sum_{n=0}^{\infty}\omega_n\frac{(-1)^n\mathrm{e}^{-\gamma x}-1}{\beta_n(s-\beta_n)}\sin(\omega_n x), \tag{3.9a}$$

where, for any function $g(t)$, $\hat{g}(s)=\int_0^\infty g(t)\exp(-st)\,\mathrm{d}t$ denotes its Laplace transform; and

$$\beta_n=-D(\omega_n^2+\gamma^2),\quad \gamma=\frac{Pe\,v}{2D},\quad \omega_n=\frac{n\pi}{L},\quad \Gamma=\sqrt{\frac{s}{D}+\gamma^2}. \tag{3.9b}$$

A benefit of working with the Laplace-transformed solution is its locality with respect to the Laplace-transformed inlet ($\hat{c}_0$) and outlet ($\hat{c}_L$) boundary concentrations. That is in contrast to the non-local solution in the time domain, which $c_0(t)$ and $c_L(t)$ enter as convolutions. This feature becomes useful in building a network solution.

3.3.1. *Steady-state solution*

If the boundary concentrations $c_0(t)$ and $c_L(t)$ have finite values at $t\to\infty$, then the steady-state solute concentration, $C_{av}^{ss}(x)$ is obtained from (3.9) by using the final value theorem, $C_{av}^{ss}(x)=\lim_{s\to 0}s\,\hat{C}_{av}(x,s)$,

$$C_{av}^{ss}(x)=\mathrm{e}^{\gamma x}\frac{\sinh[(L-x)\gamma]c_0(\infty)+\mathrm{e}^{-\gamma L}\sinh(\gamma x)c_L(\infty)}{\sinh(\gamma L)}. \tag{3.10}$$

3.3.2. *Solution for a semi-infinite vessel*

Cousins *et al.* (2013) assumed that the impedance at the network exit (i.e. at the end of the terminal arteriolar vessels) is negligible and that the network empties into an infinite reservoir, which represents the capillary microcirculation. One can model such an infinite reservoir as a semi-infinite vessel of the same diameter as the parent vessel, which would impose no resistance to the mass flow. The Laplace-transformed concentration profile in the semi-infinite vessel is (appendix A.3),

$$\hat{C}_{av}^{\infty}(x,s)=\left(\hat{c}_0(s)-\frac{c_{in}}{s}\right)\exp\left(\left(\gamma-\sqrt{\gamma^2+s/D}\right)x\right)+\frac{c_{in}}{s}. \tag{3.11}$$

4. Solute transport in bifurcating networks

The finite-length solution (3.9) describes transport along a kth generation vessel of a network, where the daughter-vessel inlet concentration $c_{0,k+1}(t)$ is imposed by the parent-vessel outlet concentration $c_{L,k}(t)$. Additionally, the daughter-vessel outlet condition is affected by the downstream impedance incurred from subsequent daughter vessels. The outlet condition in the terminal arterioles of the network may be unknown, but can be modelled by unimpeded flow into a large medium (Cousins & Gremaud 2012; Cousins *et al.* 2013). We describe this situation with the semi-infinite solution (3.11) for a vessel of the same diameter as the terminal vessels.

A nodal solution for transport throughout the tree, evaluated at bifurcation junctions, is developed by combining the tree model and the Laplace-transformed single-vessel solutions. Continuity of mass (concentration) and momentum (mass flux) is enforced at the junctions between a parent-vessel outlet and the respective daughter-vessel inlets.

4.1. *Continuity conditions at network nodes*

At each bifurcation point (node) in the kth generation of the network, continuity of mass and momentum imposes conditions

$$\hat{C}_{av,k}(L_k, s) = \hat{C}_{av,k+1}(0, s), \tag{4.1}$$

$$A_k \hat{J}_k(L_k, s) = \sum_{m=1}^{2} A_{k+1,m} \hat{J}_{k+1,m}(0, s), \tag{4.2}$$

respectively. Here $A_k = \pi a_k^2$ is the cross-sectional area of the kth generation vessel, m identifies the daughter vessel branching from the parent vessel, and J_k is the advective–dispersive mass flux across the kth interface,

$$J_k(x, t) = Pe_k v_k C_{av,k}(x, t) - D_k \nabla C_{av,k}(x, t). \tag{4.3}$$

For fractal networks, (4.2) simplifies to

$$\hat{J}_k(L_k, s) = \sum_{m=1}^{2} \alpha_m^2 \hat{J}_{k+1,m}(0, s), \quad \alpha_m = \frac{a_{k+1,m}}{a_k}. \tag{4.4}$$

4.2. *Transport in symmetrically bifurcating networks*

For symmetrically bifurcating networks, the continuity conditions (4.1) and (4.2) become

$$\hat{c}_{L,k}(s) = \hat{c}_{0,k+1,m}(s) \quad \text{and} \quad \hat{J}_k(L_k, s) = 2\alpha^2 \hat{J}_{k+1}(0, s), \tag{4.5a}$$

where

$$\left.\begin{aligned} \hat{J}_k(L_k, s) &= Pe_k v_k \hat{c}_{L,k}(s) - D_k \frac{\partial \hat{C}_{av,k}(L, s)}{\partial x}, \\ \hat{J}_{k+1}(0, s) &= Pe_{k+1} v_{k+1} \hat{c}_{0,k}(s) - D_{k+1} \frac{\partial \hat{C}_{av,k+1}(0, s)}{\partial x}. \end{aligned}\right\} \tag{4.5b}$$

Let ϕ denote the nodal concentrations, such that ϕ_k is the parent-vessel inlet concentration, ϕ_{k+1} is the concentration at the parent-vessel to daughter-vessel interface, and ϕ_{k+2} is the

daughter-vessel outlet concentration

$$\hat{\phi}_k = \hat{c}_{0,k}, \quad \hat{\phi}_{k+1} = \hat{c}_{L,k} = \hat{c}_{0,k+1}, \quad \hat{\phi}_{k+2} = \hat{c}_{L,k+1}. \tag{4.6a–c}$$

If the network consists of N_{gen} generations of vessels, then the finite vessel length solution (3.9) and the flux continuity in (4.5) give rise to a linear system of $N_{gen} - 1$ equations for the nodal concentrations,

$$\mathcal{A}_k\hat{\phi}_k + \mathcal{B}_k\hat{\phi}_{k+1} + \mathcal{F}_{k+1}\hat{\phi}_{k+2} = \mathcal{E}_k, \quad k = 1, \ldots, N_{gen}, \tag{4.7a}$$

where

$$\left.\begin{aligned}
\mathcal{A}_k &= \frac{D_k\Gamma_k \mathrm{e}^{\gamma_k L_k}}{\sinh(\Gamma_k L_k)}, \\
\mathcal{B}_k &= D_k\left[\gamma_k - \Gamma_k \coth(\Gamma_k L_k)\right] - 2\alpha^2 D_{k+1}\left[\gamma_{k+1} + \Gamma_{k+1}\coth(\Gamma_{k+1}L_{k+1})\right], \\
\mathcal{E}_k &= \sum_{n=0}^{\infty}\sum_{j=k}^{k+1} 2\omega_j^2 \frac{(2\alpha^2)^{j-k}c_{in,j}}{L_j\beta_{j,n}(s-\beta_{j,n})}\left[1 - (-1)^n \exp\left((-1)^{j-k}\gamma_j L_j\right)\right], \\
\mathcal{F}_k &= \frac{2\alpha^2 \exp\left(-\gamma_k L_k\right) D_k\Gamma_k}{\sinh(\Gamma_k L_k)}.
\end{aligned}\right\} \tag{4.7b}$$

Since ϕ_1 and $\phi_{N_{gen}+1}$ are known boundary functions, this system has $N_{gen} - 1$ unknowns $\hat{\phi}_2, \ldots, \hat{\phi}_{N_{gen}}$. It is arranged in the form of a tridiagonal matrix for each value of s,

$$\begin{bmatrix}
\mathcal{B}_1 & \mathcal{F}_2 & 0 & 0 & 0 & \cdots & 0 \\
\mathcal{A}_2 & \mathcal{B}_2 & \mathcal{F}_3 & 0 & 0 & \cdots & 0 \\
0 & \mathcal{A}_3 & \mathcal{B}_3 & \mathcal{F}_4 & 0 & \cdots & 0 \\
0 & 0 & \mathcal{A}_4 & \mathcal{B}_4 & \mathcal{F}_5 & \cdots & 0 \\
\vdots & \vdots & & \ddots & \ddots & \ddots & \vdots \\
0 & 0 & 0 & \cdots & \mathcal{A}_{N_{gen}-2} & \mathcal{B}_{N_{gen}-2} & \mathcal{F}_{N_{gen}-1} \\
0 & 0 & 0 & \cdots & 0 & \mathcal{A}_{N_{gen}-1} & \mathcal{B}_{N_{gen}-1}
\end{bmatrix}
\begin{bmatrix}
\hat{\phi}_2 \\ \hat{\phi}_3 \\ \hat{\phi}_4 \\ \hat{\phi}_5 \\ \hat{\phi}_6 \\ \vdots \\ \hat{\phi}_{N_{gen}}
\end{bmatrix}
=
\begin{bmatrix}
\mathcal{E}_1 - \mathcal{A}_1\hat{\phi}_1 \\ \mathcal{E}_2 \\ \mathcal{E}_3 \\ \mathcal{E}_4 \\ \mathcal{E}_5 \\ \vdots \\ \mathcal{E}_{N_{gen}-1} - \mathcal{F}_{N_{gen}}\hat{\phi}_{N_{gen}+1}
\end{bmatrix} \tag{4.8}$$

and solved using the Thomas algorithm (Datta 2010).

If a network of finite-length vessels ends with a set of semi-infinite vessels at its last generation to incorporate the outflow condition, then

$$\left.\begin{aligned}
\mathcal{A}_{N_{gen}-1} &= \frac{D_{N_{gen}-1}\Gamma_{N_{gen}-1}}{\sinh(\Gamma_{N_{gen}-1}L_{N_{gen}-1})}\exp\left(\gamma_{N_{gen}-1}L_{N_{gen}-1}\right), \\
\mathcal{B}_{N_{gen}-1} &= D_{N_{gen}-1}[\gamma_{N_{gen}-1} - \Gamma_{N_{gen}-1}\coth(\Gamma_{N_{gen}-1}L_{N_{gen}-1})] - 2\alpha^2(U_{N_{gen}} - D_{N_{gen}}\varpi), \\
\mathcal{E}_{N_{gen}-1} &= -\frac{\alpha^2 c_{in,N_{gen}}}{s}\varpi - 2\omega_{N_{gen}-1}^2 L_{N_{gen}-1}c_{in,N_{gen}-1}\sum_{n=0}^{\infty}\frac{1-(-1)^n\exp\left(\gamma_{N_{gen}-1}L_{N_{gen}-1}\right)}{\beta_{N_{gen}-1,n}(s-\beta_{N_{gen}-1,n})}, \\
\mathcal{F}_{N_{gen}} &= 0,
\end{aligned}\right\} \tag{4.9}$$

where $\varpi = \gamma_{N_{gen}} - \sqrt{\gamma_{N_{gen}}^2 + s/D_{N_{gen}}}$.

5. Simulation results

5.1. *Solute transport in a single vessel*

Distinct regimes of dispersive transport in a vessel are characterized by the Péclet number $Pe = v_c L_c/D_c$, the ratio of the advective and dispersive time scales. Figure 1 exhibits temporal snapshots of concentration profiles C_{av}/c_0 for $Pe = 0.01$, 0.1, 1.0 and 10. Recall that here and below all the quantities are dimensionless, as defined in (3.6*a–j*). The profiles for $Pe < 1$ are similar because dispersion (spreading of the front) dominates advection (translation of the front). The dispersive forces, therefore, drive the vessel saturation rate and small changes in the advective forces are not visible. As the Péclet number exceeds 1, the transport front becomes steeper, reflecting the increase in advective strength.

The numerical error in our solution can stem only from numerical inversion of the Laplace transforms, which we have carried out with the DeHoog algorithm implemented by Hollenbeck (1998). Any numerical inversion algorithm loses accuracy near asymptotes, at early (large s) and late (small s) times. The errors emerge as a result of numerical roundoff while performing operations with very large or small numbers (small s correspond to large t, and *vice versa*). Additionally, they can vary with Pe (Zimmerman, Jankowski & Tartakovsky 2016). These errors can be controlled either numerically by using systems/software that can handle larger floating point operations or analytically by evaluating the inverse Laplace transforms for small and large s, as is done in (3.10). Figure 1 demonstrates the agreement between the analytical solution for $C_{av}(x, t)$ and its counterpart obtained by numerical inversion of the Laplace transform $\hat{C}_{av}(x, s)$, for all values of Pe considered.

5.2. *Model verification*

The data indicate that the ratio between vessel radius and vessel length is similar for both small and large vessels in the arteriolar network. We therefore assume that, in each generation k, the length (L_k) and radius (a_k) of each vessel differ by the same constant (λ),

$$L_k = \frac{a_k}{\lambda}, \quad 0 < \lambda < 1. \tag{5.1}$$

To verify our network solution (4.8), we consider a network that is functionally equivalent to a single vessel. The network consists of $N_{gen} = 100$ generations and has the same total length L_{net} as the single vessel, $L_{net} = L = 1$. Since the total network length is

$$L_{net} = \sum_{k=1}^{N_{gen}} L_k = \sum_{k=1}^{N_{gen}} \frac{a_k}{\lambda}, \tag{5.2}$$

it follows from (2.4) that all vessels in the network have the aspect ratio

$$\lambda = \frac{a_1}{L_{net}} \sum_{k=1}^{\eta} \alpha^{k-1}. \tag{5.3}$$

The total cross-sectional area of each generation's vessel in the symmetrically bifurcating network is kept constant by choosing $\alpha = 1/\sqrt{2}$. According to (2.7), this also ensures that the average flow velocity remains the same across all generations, $v_k = v_{k+1}$. The dispersion coefficient changes with velocity and vessel radius, in accordance with (3.4*a–c*). To facilitate verification of the semi-analytical network solution against the

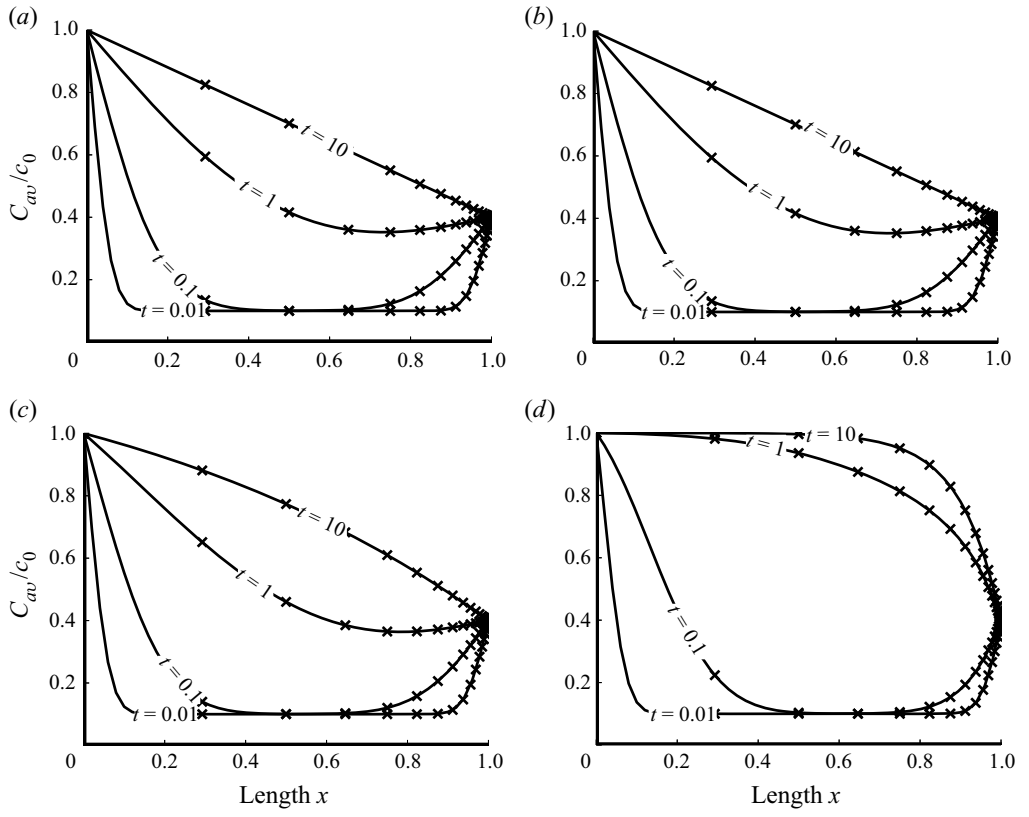

FIGURE 1. Temporal snapshots of the normalized concentration profiles, $C_{av}(x, t)/c_0$, along the vessel, $0 \leq x \leq 1$, for several values of the Péclet number, Pe. The profiles are computed, alternatively, with the analytical solution provided in appendix A (solid lines) and its counterpart obtained by numerical inversion of (3.9). The input concentrations are normalized with c_0, such that $c_L/c_0 = 0.4$ and $c_{in}/c_0 = 0.1$. The network parameters are set to $N_{gen} = 100$ and $\lambda = 0.1$. (*a*) $Pe = 0.01$. (*b*) $Pe = 0.1$. (*c*) $Pe = 1$. (*d*) $Pe = 10$.

analytical single-vessel solution, we use the constant dispersion coefficient for all vessel generations, $D_k = D_{k+1}$. Transport in the network thus constructed should behave as though it were taking place in a single vessel of equivalent length and cross-sectional area. It is worthwhile emphasizing that this network does not represent the arterial tree; it merely serves to verify our network solution (4.8).

By construction, the concentration profiles are identical to those in figure 1. The relative error between the network solution (4.8) and the single-vessel solution (3.9), $\varepsilon(x, t) = (C_{network} - C_{single})/C_{single}$, is displayed in figure 2 for several values of the network Péclet number $Pe_{net} = v_c L_{tot}/D_c$. For all the scenarios considered, the error does not exceed 0.12 %. It decreases with both time t and Pe.

5.3. *Analysis of a representative arteriolar network*

A rigorous model of the human cardiovascular system should account for uneven bifurcation between parent and daughter vessels. The latter would require a solution for the impedance and pressure profiles of the network (Cousins & Gremaud 2012), as well as the changes in viscosity due to the Fahraeus–Lindqvist effect (Sriram *et al.* 2014*a*). We present a methodology for deriving such a generalized model. Additionally, the dynamics

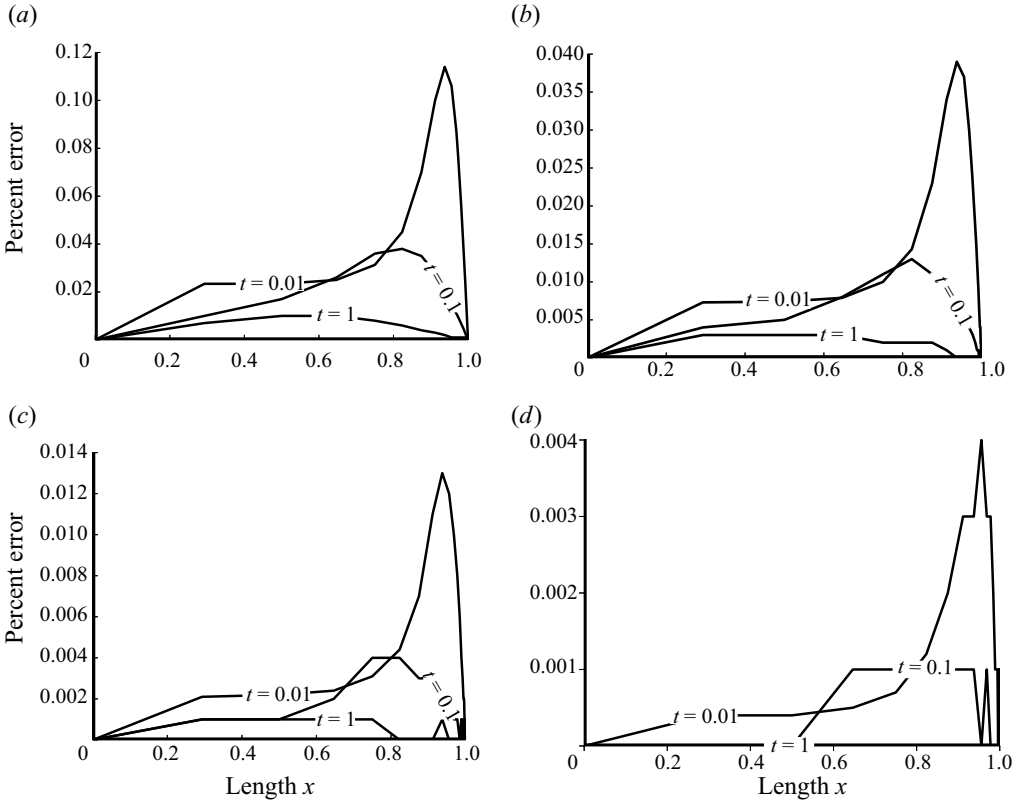

FIGURE 2. Relative error of the network solution. The model parameters are set to $N_{gen} = 100$, $\lambda = 0.1$, $c_L/c_0 = 0.4$ and $c_{in}/c_0 = 0.1$. (*a*) $Pe = 0.01$. (*b*) $Pe = 0.1$. (*c*) $Pe = 1$. (*d*) $Pe = 10$.

of an evenly bifurcating network may inform the choice of more complex models. To demonstrate the transport behaviour in the evenly bifurcating arteriolar network, we consider two cases: a constant inlet and single-pulse inlet flow. The first utilizes a constant inlet boundary condition with no initial concentration to illustrate the development of a steady-state flow. The second implements a step function at the inlet boundary with no initial concentration to represent a single pulse of solute transiting through the network. In both cases, the unimpeded outflow boundary condition is imposed at the network exit, i.e. the vessel exit empties into a semi-infinite vessel of the same diameter.

Table 1 collates the vessel geometric characteristics found throughout the human arterial vasculature. Our network model is built from the arteriolar parameters presented in table 2. For the exponent $\zeta = 2.76$, representative of the human cardiovascular system (Olufsen 1999), (2.4) predicts the daughter-to-parent radius ratio $\alpha = 0.778$. (This value is slightly above the values reported in table 2, which can be attributed to our choice of the symmetrical branching.) We set $\lambda = 0.005$, which is the median value of those reported in table 2 and is in agreement with its counterpart for the arteriolar vessels in table 1.

The flow rate and vessel radius in the first arteriolar vessel generation ($k = 1$) is selected from table 2 to be $v_1 = 10$ mm s^{-1} and $a_1 = 40$ μm, respectively. The corresponding diffusion coefficient is chosen as $D_m = 10^{-4}$ mm^2 s^{-1}. We select the minimum vessel radius $a_{min} = 8$ μm, below which our arteriolar network is terminated and the unimpeded outflow condition is imposed. When used in conjunction with the fractal model of § 2,

Level	v (cm s^{-1})	L (cm)	a (cm)	α	λ
1	0.97	1.2	0.004	—	0.0033
2	0.62	0.6	0.0025	0.625	0.0042
3	0.39	0.2	0.0015	0.600	0.0075
4	0.22	0.1	0.00075	0.500	0.0075

TABLE 2. Dimensions of, and flow velocity in, vessels of the arteriolar network (Popel & Gross 1979). Here, $\lambda = a/L$ is the ratio between the radius (a) and length (L) of a vessel; and $\alpha = a_d/a_p$ is the ratio between the radii of the daughter (a_d) and parent (a_p) vessels.

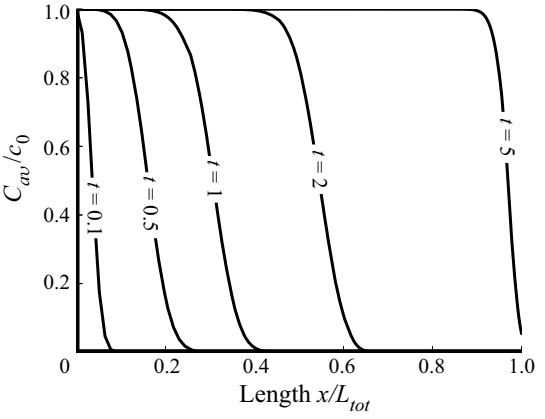

FIGURE 3. Temporal snapshots of the normalized concentration profiles, $C_{av}(x, t)/c_0$, along the length of the network with constant inlet concentration c_0 and initial concentration $c_{in} = 0$. The parameter values are set to $\lambda = 0.005$, $\alpha = 0.778$, $a_1 = 0.04$ mm, $u_1 = 10$ mm s^{-1} and $D_m = 10^{-4}$ mm^2 s.

these vessel geometries and parameters result in a symmetrically bifurcating arteriolar tree with $N_{gen} = 8$ generations and $a_{N_{gen}} = 6.9$ μm.

Figure 3 shows the propagation of the concentration front in the described arteriolar tree with zero initial concentration, $c_{in} = 0$, a fixed inlet concentration, c_0, and the unimpeded outflow condition (4.9). The Péclet numbers observed in the arteriolar network are large, leading to the sharp concentration front at all times. At early times, the front develops its shape and widens. As the concentration front transits to the downstream vessels, the Péclet number of the daughter generations decreases, because $\alpha > 1/\sqrt{2}$, and so the collective cross-sectional area of each generation is greater than that of the parent generation. In a single vessel with constant cross-sectional area, a decrease in the Péclet number results in the dispersion phenomenon having a greater effect on the transport front of the solute. This can be inferred from the flow regime comparisons in figure 1. A lower Péclet number results in a more gradual concentration front when comparing vessels of similar geometry. Counterintuitively, the network presented in figure 3 has a concentration front that steepens as it transits toward the network exit. This phenomenon is due to reduced velocity of flow in each successive generation, which causes the concentration front to 'bunch up' similar to a traffic jam. As will be seen shortly, this effect is more pronounced with the single pulse inlet boundary condition.

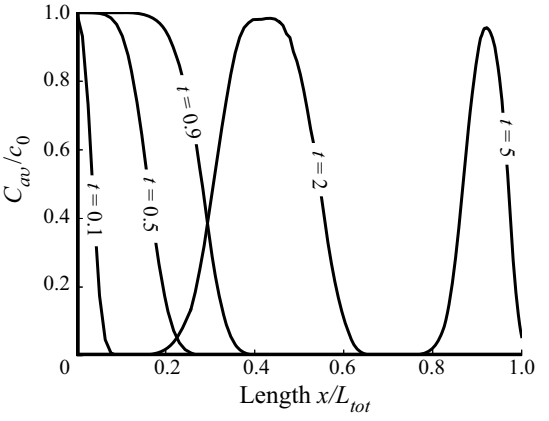

FIGURE 4. Temporal snapshots of the normalized concentration profiles, $C_{av}(x, t)/\mathcal{A}$, along the length of the network with initial concentration $c_{in} = 0$ and the pulse inlet concentration (5.4). The parameter values are set to $\lambda = 0.005$, $\alpha = 0.778$, $a_1 = 0.04$ mm, $u_1 = 10$ mm s^{-1} and $D_m = 10^{-4}$ mm^2 s^{-1}.

The second case is defined by a single pulse inlet boundary condition, zero initial concentration and the unimpeded flow boundary condition at the vessel exit. The pulse inlet boundary condition is a step function given by the relation

$$c_0(t) = \mathcal{A}[H(t - t_1) - H(t - t_2)]. \tag{5.4}$$

Here, t_1 and t_2 are the times at which the pulse starts and ends, $\mathcal{A}$ is the concentration of the pulse and $H(\cdot)$ is the Heaviside step function. The Laplace transform of (5.4) is

$$\hat{c}_0(s) = \frac{\mathcal{A}}{s}\left[\mathrm{e}^{-t_1 s} - \mathrm{e}^{-t_2 s}\right]. \tag{5.5}$$

Figure 4 shows a one-second pulse introduced at the network's entrance. The network used in this case is geometrically and physiologically consistent with the constant inlet boundary condition case described in figure 3. The regime that resulted in the steepening of the transport front in figure 3 is also observable in figure 4. However, now, the trailing edge of the pulse 'catches up' with its leading edge, illustrating the traffic jam behaviour. At first glance, the solute appears to be lost because the area under the curve decreases as the pulse transits down the network. This phenomenon is due to the increase in cross-sectional area of each successive vessel generation as the pulse moves towards the network exit. Conversely, networks with $\alpha < 1/\sqrt{2}$ induce transport fronts to grow wider as the Péclet number increases and the total cross-sectional area decreases with each successive generation.

6. Conclusions

We developed an analytical model for advection–dispersion transport in a fractal bifurcating network. The solution was evaluated for the values of geometric and topological parameters relevant to the human arteriolar vasculature. The accuracy of our solution, i.e. the errors associated with numerical inversion of Laplace transforms, was investigated over the physiologically relevant range of the parameter values.

Our analysis revealed that solute transport through an evenly bifurcating network is controlled, to a large extent, by the ratio (α) between the radii of the daughter

and parent vessels. Specifically, $\alpha = 1/\sqrt{2}$ identifies an inflection point at which the transport behaviour changes. A network with $\alpha > 1/\sqrt{2}$ gives rise to a transport front that bunches up from a linear perspective of the vascular network. A network with $\alpha = 1/\sqrt{2}$ corresponds to Da Vinci's law, according to which the cross-sectional area of a parent tree branch (or tree trunk) is equal to the total cross-sectional area of the daughter branches; this regime is applicable to transport in xylem (Minamino & Tateno 2014). Networks with $\alpha < 1/\sqrt{2}$ induce transport fronts to widen as the Péclet number increases and the total cross-sectional area decreases with each successive generation.

To focus on the effects of network topology on transport characteristics, we neglected many key features of transport in microcirculation such as a lattice-like structure of the capillary bed, radial transport through vessel walls, and non-Newtonian behaviour of blood in small vessels. In this sense, the relevance of our model to microcirculation comes with important caveats. It should be used as an abstracted representation of solute transport in the arteriolar network just upstream of the capillary bed, where the network exhibits fractal bifurcation patterns. Our single-vessel solutions can be replaced with the solutions of Zimmerman *et al.* (2018) to account for diffusive losses through the vessel wall. They can be generalized further by replacing the Hagen–Poiseuille profile characteristic of Newtonian fluids with its counterparts resulting from the two-phase Newtonian (Sriram *et al.* 2012) or non-Newtonian (Sriram, Intaglietta & Tartakovsky 2014*b*) models of blood in microcirculation. Finally, one can follow Cousins & Gremaud (2012) to accommodate asymmetric bifurcations at each vessel junction, and Sriram *et al.* (2014*a*) to account for viscosity changes due to the Fahraeus–Lindqvist effect.

Our results are also applicable to transport in a variety of other environments such as nutrient transport in floral structures (Mäkelä 2002), fungal networks (Heaton *et al.* 2012*b*) and drug delivery (Shipley & Chapman 2010). Our model can be extended to networks with more than two daughter vessels branching per junction. Small modifications to the branching parameters, can describe a wide variety of other fractal networks.

Acknowledgements

This work was supported in part by Air Force Office of Scientific Research under award number FA9550-18-1-0474.

Declaration of interests

The authors report no conflict of interest.

Appendix A. Derivation of single-vessel solutions

We use the Green's function method to derive an analytical solution to (3.7) and (3.8*a–c*), and the Laplace transformation to obtain its counterpart for a semi-infinite vessel.

A.1. *Greens' function for advection–dispersion equation*

The Green's function in (3.7) and (3.8*a–c*), $G(x, \xi, t-\tau)$, satisfies an adjoint equation

$$\frac{\partial G}{\partial \tau} = D\frac{\partial^2 G}{\partial \xi^2} - Pe\, v\, \frac{\partial G}{\partial \xi} + \delta(x-\xi)\delta(t-\tau), \quad x, \xi \in (0, L), \quad t > \tau > 0; \tag{A 1}$$

subject to homogeneous initial and boundary conditions

$$G(x,t;\xi,0)=0,\quad G(x,t;0,\tau)=0,\quad G(x,t;L,\tau)=0, \tag{A 2a–c}$$

where $\delta(\cdot)$ is the Dirac delta function. The solution of this boundary-value problem is

$$G(x,\xi,t-\tau)=2H(t-\tau)\sum_{n=0}^{\infty}\exp\left(\beta_n(t-\tau)-\gamma(\xi-x)\right)\sin(\omega_n x)\sin(\omega_n\xi), \tag{A 3}$$

where $H(\cdot)$ is the Heaviside function; and the constants β_n, γ and ω_n are defined in (3.9*b*).

A.2. *Solution to advection–dispersion equation*

The solution to (3.7) and (3.8*a–c*) is written in terms of the Green's function $G(x,\xi,t-\tau)$ in (A 3) as

$$C_{av}(x,t)=\int_0^L c_{in}G(x,\xi,t)\,\mathrm{d}\xi+\int_0^t\left[c_0(\tau)\frac{\partial G}{\partial\xi}(x,0,t-\tau)-c_L(\tau)\frac{\partial G}{\partial\xi}(x,L,t-\tau)\right]\mathrm{d}\tau. \tag{A 4}$$

For the spatially uniform initial concentration c_{in}, substituting (A 3) into (A 4) and taking the Laplace transformation of the resulting expression, we obtain

$$\hat{C}_{av}(x,s)=\frac{2D}{L}\mathrm{e}^{\gamma x}\sum_{n=0}^{\infty}\frac{\omega_n\sin(\omega_n x)}{s-\beta_n}\left[c_{in}\frac{(-1)^n\mathrm{e}^{-\gamma L}-1}{\beta_n}+\hat{c}_0(s)-(-1)^n\mathrm{e}^{-\gamma L}\hat{c}_L(s)\right]. \tag{A 5}$$

Since (Hansen 1975, equations (14.3.8) and (14.3.9))

$$\sum_{n=0}^{\infty}\frac{n}{n^2a^2+b^2}\sin(nX)=\frac{\pi}{2a^2}\frac{\sinh[(\pi-X)b/a]}{\sinh(\pi b/a)} \tag{A 6}$$

and

$$-\sum_{n=0}^{\infty}\frac{(-1)^n n}{n^2a^2+b^2}\sin(nX)=\frac{\pi}{2a^2}\frac{\sinh(bX/a)}{\sinh(\pi b/a)}, \tag{A 7}$$

(A 5) gives rise to (3.9).

Single-vessel solutions may be developed without the use of the Green's function method, as was done in the case of the semi-infinite vessel solution in § 3. In some cases these other methods may even present a more concise derivation. The Green's functions are utilized here for the purpose of presenting a base on which higher-dimensional solutions may be developed in future work. Specifically, the Green's function for a multi-dimensional advection–diffusion equation (e.g. in cylindrical coordinates) is given by the product of the corresponding one-dimensional Green's functions such as (A 3).

A.3. *Solution for a semi-infinite vessel*

In the case of a semi-infinite vessel, the domain of definition of (3.7), $(0,L)$, is replaced with $(0,\infty)$, and the last boundary condition in (3.8*a–c*) with $C_{av}(\infty,t)=c_{in}$.

The Laplace transform of (3.7) is

$$s\hat{C}_{av}(x,s) - c_{in} = \frac{\mathrm{d}^2\hat{C}_{av}(x,s)}{\mathrm{d}x^2} - \frac{Pe\,v}{D}\frac{\mathrm{d}\hat{C}_{av}(x,s)}{\mathrm{d}x}. \tag{A 8}$$

A solution to this equation is a linear combination of homogeneous and particular solutions,

$$\hat{C}_{av}(x,s) = \hat{C}_h(x,s) + \hat{C}_p(x,s). \tag{A 9}$$

The former satisfies

$$s\hat{C}_h(x,s) = \frac{\mathrm{d}^2\hat{C}_h(x,s)}{\mathrm{d}x^2} - \frac{Pe\,v}{D}\frac{\mathrm{d}\hat{C}_h(x,s)}{\mathrm{d}x} \tag{A 10}$$

and is given by

$$\hat{C}_h(x,s) = a_1\mathrm{e}^{\theta_- x} + a_2\mathrm{e}^{\theta_+ x}, \quad \theta_\pm = \gamma \pm \sqrt{\gamma^2 + s/D}. \tag{A 11a,b}$$

A particular solution to (A 8), obtained either by direct inspection of (A 8) or with the method of variation of parameters, is

$$\hat{C}_p(x,s) = \frac{c_{in}}{s}. \tag{A 12}$$

Accounting for the boundary conditions to compute the constants of integration a_1 and a_2, we obtain (3.11).

REFERENCES

Adam, J. A. 2011 Blood vessel branching: beyond the standard calculus problem. *Math. Mag.* **84** (3), 196–207.

Aris, R. 1956 On the dispersion of a solute in a fluid flowing through a tube. *Proc. R. Soc. Lond.* A **235** (1200), 67–77.

Beard, D. A. & Bassingthwaighte, J. B. 2000 Advection and diffusion of substances in biological tissues with complex vascular networks. *Ann. Biomed. Engng* **28** (3), 253–268.

Beard, D. A. & Bassingthwaighte, J. B. 2001 Modeling advection and diffusion of oxygen in complex vascular networks. *Ann. Biomed. Engng* **29** (4), 298–310.

Berg, M., Davit, Y., Quintard, M. & Lorthois, S. 2020 Modelling solute transport in the brain microcirculation: is it really well mixed inside the blood vessels? *J. Fluid Mech.* **884**, A39.

Bruderer, C. & Bernabé, Y. 2001 Network modeling of dispersion: transition from Taylor dispersion in homogeneous networks to mechanical dispersion in very heterogeneous ones. *Water Resour. Res.* **37** (4), 897–908.

Cabrales, P., Tsai, A. G., Winslow, R. M. & Intaglietta, M. 2005 Extreme hemodilution with PEG-hemoglobin vs. PEG-albumin. *Am. J. Physiol. Heart. Circ. Physiol.* **289**, H2392–H2400.

Cairney, J. W. G. 1992 Translocation of solutes in ectomycorrhizal and saprotrophic rhizomorphs. *Mycological Res.* **96** (2), 135–141.

Cousins, W. & Gremaud, P. A. 2012 Boundary conditions for hemodynamics: the structured tree revisited. *J. Comput. Phys.* **231** (18), 6086–6096.

Cousins, W., Gremaud, P. A. & Tartakovsky, D. M. 2013 A new physiological boundary condition for hemodynamics. *SIAM J. Appl. Maths* **73** (3), 1203–1223.

Dailey, S. E., Dysart, C. B., Langan, D. R., Slye, M. J., Nuttal, G. A., Schrader, L. M., Williams, B. A. & Oliver, W. C. 2005 An in vitro study comparing the effects of Hextend, Hespan, normal saline, and lactated Ringer's solution on thrombelastography and the activated partial thromboplastin time. *Cardiothorac. Vasc. Anesth.* **19** (3), 358–361.

DATTA, B. N. 2010 *Numerical Linear Algebra and Applications*, vol. 116. SIAM.

FUNG, Y. C. & TANG, H. T. 1975 Longitudinal dispersion of tracer particles in the blood flowing in a pulmonary alveolar sheet. *J. Appl. Mech.* **42** (3), 536–540.

GENTILE, F., FERRARI, M. & DECUZZI, P. 2008 The transport of nanoparticles in blood vessels: the effect of vessel permeability and blood rheology. *Ann. Biomed. Engng* **36** (2), 254–261.

GISLADOTTIR, V. R., ROUBINET, D. & TARTAKOVSKY, D. M. 2016 Particle methods for heat transfer in fractured media. *Transp. Porous Med.* **115** (2), 311–326.

GOLDMAN, D. 2008 Theoretical models of microvascular oxygen transport to tissue. *Microcirculation* **15** (8), 795–811.

GOLDMAN, D. & POPEL, A. S. 2000 A computational study of the effect of capillary network anastomoses and tortuosity on oxygen transport. *J. Theor. Biol.* **206** (2), 181–194.

GREEN, H. D. 1944 Circulation: physical principles. In *Medical Physics* (ed. O. Glasser). The Year Book Publishers, Inc.

HANSEN, E. R. 1975 *A Table of Series and Products*. Prentice-Hall.

HEATON, L. L. M., LÓPEZ, E, MAINI, P. K., FRICKER, M. D. & JONES, N. S. 2012*a* Advection, diffusion, and delivery over a network. *Phys. Rev.* E **86**, 021905.

HEATON, L., OBARA, B., GRAU, V., JONES, N. S., NAKAGAKI, T., BODDY, L. & FRICKER, M. D. 2012*b* Analysis of fungal networks. *Fungal Biol. Rev.* **26** (1), 12–29.

HELLUMS, J. D., NAIR, P. K., HUANG, N. S. & OHSHIMA, N. 1995 Simulation of intraluminal gas transport processes in the microcirculation. *Ann. Biomed. Engng* **24** (1), 1–24.

HOLLENBECK, K. J. 1998 INVLAP.M: a Matlab function for numerical inversion of Laplace transforms by the de Hoog algorithm. http://www.isva.dtu.dk/staff/karl/invlap.htm.

JENNINGS, D. H. 1987 Translocation of solutes in fungi. *Biol. Rev.* **62** (3), 215–243.

KOFFIE, R. M., FARRAR, C. T., SAIDI, L.-J., WILLIAM, C. M., HYMAN, B. T. & SPIRES-JONES, T. L. 2011 Nanoparticles enhance brain delivery of blood–brain barrier-impermeable probes for in vivo optical and magnetic resonance imaging. *Proc. Natl Acad. Sci. USA* **108** (46), 18837–18842.

LEE, J.-S. & FUNG, Y.-C. 1971 Flow in nonuniform small blood vessels. *Microvasc. Res.* **3** (3), 272–287.

MÄKELÄ, A. 2002 Derivation of stem taper from the pipe theory in a carbon balance framework. *Tree Physiol.* **22** (13), 891–905.

MCCULLOH, K. A., SPERRY, J. S. & ADLER, F. R. 2003 Water transport in plants obeys Murray's law. *Nature* **421** (6926), 939–942.

MINAMINO, R. & TATENO, M. 2014 Tree branching: Leonardo da Vinci's rule versus biomechanical models. *PloS One* **9** (4), e93535.

OLUFSEN, M. S. 1999 Structured tree outflow condition for blood flow in larger systemic arteries. *Am. J. Physiol. Heart Circ. Physiol.* **276** (1), H257–H268.

OLUFSEN, M. S., PESKIN, C. S., KIM, W. Y., PEDERSEN, E. M., NADIM, A. & LARSEN, J. 2000 Numerical simulation and experimental validation of blood flow in arteries with structured-tree outflow conditions. *Ann. Biomed. Engng* **28** (11), 1281–1299.

POPEL, A. S. & GROSS, J. F. 1979 Analysis of oxygen diffusion from arteriolar networks. *Am. J. Physiol. Heart Circ. Physiol.* **237** (6), H681–H689.

PRIES, A. R., SECOMB, T. W., GAEHTGENS, P. & GROSS, J. F. 1990 Blood flow in microvascular networks. Experiments and simulation. *Circ. Res.* **67** (4), 826–834.

ROUBINET, D., DE DREUZY, J.-R. & TARTAKOVSKY, D. M. 2013 Particle-tracking simulations of anomalous transport in hierarchically fractured rocks. *Comput. Geosci.* **50**, 52–58.

SACK, L. & HOLBROOK, N. M. 2006 Leaf hydraulics. *Annu. Rev. Plant Biol.* **57**, 361–381.

SARPKAYA, T. 1966 Experimental determination of the critical Reynolds number for pulsating Poiseuille flow. *J. Basic Engng* **88** (3), 589–598.

SHAW, S. & MURTHY, P. V. S. N. 2010 Magnetic targeting in the impermeable microvessel with two-phase fluid model–Non-Newtonian characteristics of blood. *Microvasc. Res.* **80**, 209–220.

SHIPLEY, R. J. & CHAPMAN, S. J. 2010 Multiscale modelling of fluid and drug transport in vascular tumours. *Bull. Math. Biol.* **72** (6), 1464–1491.

SRIRAM, K., INTAGLIETTA, M. & TARTAKOVSKY, D. M. 2014*a* Hematocrit dispersion in asymmetrically bifurcating vascular networks. *Am. J. Physiol. Heart Circ. Physiol.* **307** (11), H1576–H1586.

SRIRAM, K., INTAGLIETTA, M. & TARTAKOVSKY, D. M. 2014*b* Non-Newtonian flow of blood in arterioles: consequences for wall shear stress measurements. *Microcirculation* **21** (7), 628–639.

SRIRAM, K., VAZQUEZ, B. Y. S., TSAI, A. G., CABRALES, P., INTAGLIETTA, M. & TARTAKOVSKY, D. M. 2012 Autoregulation and mechanotransduction control the arteriolar response to small changes in hematocrit. *Am. J. Physiol. Heart Circ. Physiol.* **303** (9), H1096–H1106.

UYLINGS, H. B. M. 1977 Optimization of diameters and bifurcation angles in lung and vascular tree structures. *Bull. Math. Biol.* **39** (5), 509–520.

WOMERSLEY, J. R. 1955 Method for the calculation of velocity, rate of flow and viscous drag in arteries when the pressure gradient is known. *J. Physiol.* **127** (3), 553.

YOUNG, J. H., EVERT, R. F. & ESCHRICH, W. 1973 On the volume-flow mechanism of phloem transport. *Planta* **113** (4), 355–366.

ZAMIR, M. 1988 The branching structure of arterial trees. *Comments Theor. Biol.* **1**, 15–37.

ZIMMERMAN, R. A., JANKOWSKI, T. A. & TARTAKOVSKY, D. M. 2016 Analytical models of axisymmetric reaction-diffusion phenomena in composite media. *Intl J. Heat Mass Transfer* **99**, 425–431.

ZIMMERMAN, R. A., SEVERINO, G. & TARTAKOVSKY, D. M. 2018 Hydrodynamic dispersion in a tube with diffusive losses through its walls. *J. Fluid Mech.* **837**, 546–561.

ZIMMERMAN, R. A., TSAI, A. G., INTAGLIETTA, M. & TARTAKOVSKY, D. M. 2019 A mechanistic analysis of possible blood transfusion failure to increase circulatory oxygen delivery in anemic patients. *Ann. Biomed. Engng* **47** (4), 1094–1105.